NUMERICAL SIMULATION FOR SEDIMENT TRANSPORT IN SHEETFLOW REGIME USING DEM-MPS

E. Harada[1], H. Ikari [1], Y. Shimizu [1] and H. Gotoh [1]

ABSTRACT: A regime of highly concentrated sediment transport, or sheetflow, which is observed around coastal surf-zone, has significant impact on a coastal process. However, it is difficult to directly measure an inner-structure of the sheetflow from experimental measurement, because the sheetflow is a phenomenon with highly concentrated fast granular flows. As well as, because the sheetflow is a phenomenon in strong non-linear multi-phase flow, an implementation of numerical simulation is still a challenging problem. In the present research, as one way to the understanding of surf-zone sheetflow mechanism, the numerical simulation for the sheetflow sediment transport is performed in the uniform flow condition, by reference to the previous experimental results. In the present numerical model, to simulate sheetflow under open channel flow with free surface with a high degree of accuracy, the enhanced Moving Particle Semi-implicit (MPS) method, which is one of the Lagrangian models, is used to the liquid phase. On the other hand, the Distinct Element Method (DEM) is applied to the solid-particle phase to track individual particle motion. By coupling these methods, the three-dimensional Lagrange-Lagrange coupling model is prepared for the purpose of computational investigation of an inner structure of the sheetflow layer. From the present numerical results, the significant collision frequency between particles is found in the sheetflow layer including a high sediment concentration, concurrently, simulation result indicates inter-particle force by particle collision is the key factor to reveal the sediment transport mechanism in the sheetflow layer, from the viewpoint of computational sediment transport.

Keywords:sheetflow, Distinct Element Method (DEM), Moving Particle Semi-implicit (MPS) method, inter-particle collision.

INTRODUCTION

A sheetflow is one of regimes for sediment transport, which is usually observed around coastal surf zones. Massive sediment is transported under the sheetflow regime, thus it is well known the sheetflow has great impact on coastal processes. Understandings of the mechanism of sheetflow are indispensable to manage coastal topographic change, especially in controlling cross section from onshore to offshore direction. In the sheetflow regime, sediment particles are transported with a high velocity and high condense, its physical process shows in nature strongly non-linear phenomena. Therefore, investigations of the mechanism of sediment transport in the sheetflow regime are quite difficult in both experimental measurements and numerical simulations, and a lot of uncertainties for an inner structure of the sheetflow are remaining.

In the past studies related to the sheetflow in surf zones, some of them investigate the mechanism of sheetflow numerically using Lagrangian model such as the DEM (distinct element method; Cundall and Strack, 1979), and the sediment transport is discussed from an individual solid particle scale (e.g., Drake and Calantoni, 2001; Calantoni et al., 2006; Harada and Gotoh, 2008; Harada et al., 2015). However, a numerical resolution of hydrodynamic force around each solid particle is not enough, satisfactory investigations regarding the sheetflow in surf zones have not been implemented from the scale level of representative solid particle, or a particle diameter. Also, effects of momentum exchange by wave breakings is omitted or is not satisfactorily estimated.

In the present study, the numerical simulation for sediment transport under the sheetflow regime is performed using the DEM-MPS coupling model by Gotoh et al. (2012) and Tsuruta (2014), and the inner structure of sheetflow layer is investigated numerically with using the fluid resolution same as the diameter of DEM solid particle. In addition, to simulate a free surface flow with fluctuations induced by a small scale wave breakings accurately, the enhanced MPS (moving particle semi-implicit) is employed. (Gotoh and Okayasu, 2017). Note that in the present study, the numerical simulation for sheet flow formed on the open channel is carried out under the uniform flow, as the first step of investigation of sheetflow structure in surf zones. By comparing the present numerical results with the previous experimental results by Larcher et al. (2007), verification of the present numerical results for sheet flow is carried out from the averaged velocity and

[1] Department of Civil and Earth Resources Engineering, Kyoto University, Katsura Campus, Nishikyo-ku, Kyoto, 615-8540, JAPAN

fluctuated velocity of solid particle motion. Then, the inner structure of sheetflow is investigated. As the result, significant contributions of inter-particle collisions to the sediment transport in sheetflow regime is suggested.

NUMERICAL MODEL

In this study, DEM-MPS coupling model (Gotoh et al., 2012; Tsuruta, 2014) is adopted in reproduction of sheetflow. The DEM-MPS coupling model is recently applied to the coastal morphological change problem (e.g., Harada et al., 2019). The liquid phase is solved by an enhanced MPS method (Gotoh and Okayasu, 2017), which benefits from a set of previously developed refined schemes. The solid phase is discretized and tracked in the framework of DEM (Cundall and Strack, 1979). The liquid and solid phases are weakly coupled through the projection of physical quantities and the imposition of an interaction force term.

Governing Equations

The equations governing the fluid flows (or motions of mixture phase) correspond to continuity and Navier-Stokes equations:

$$\frac{D\bar{\rho}}{Dt} + \bar{\rho}\nabla \cdot \bar{\boldsymbol{u}} = 0 \tag{1}$$

$$\bar{\rho}\frac{D\bar{\boldsymbol{u}}}{Dt} = -\nabla p + \bar{\mu}\nabla^2\bar{\boldsymbol{u}} + \bar{\rho}\boldsymbol{g} + \boldsymbol{F}_{p\text{int}} \tag{2}$$

where D/Dt refers to Lagrangian time derivative, ρ signifies density, $\boldsymbol{u}$ represents velocity vector, p denotes pressure, μ is dynamic viscosity and $\boldsymbol{g}$ symbolizes gravitational acceleration vector; $\boldsymbol{F}_{p\text{int}}$ corresponds to solid-liquid interaction force vector. The bar "–" stands for projected variables estimated as:

$$\bar{\rho} = \rho_l\left(1 - \int_V \varphi_{sl}\,dV\right) + \rho_s\int_V \varphi_{sl}\,dV \tag{3}$$

$$\bar{\mu} = \mu_l\left(1 - \int_V \varphi_{sl}\,dV\right) + \mu_s\int_V \varphi_{sl}\,dV \tag{4}$$

$$\bar{\boldsymbol{u}} = \boldsymbol{u}_l\left(1 - \int_V \varphi_{sl}\,dV\right) + \left(\boldsymbol{u}_s + \boldsymbol{r}_{sl}\times\boldsymbol{\omega}_s\right)\int_V \varphi_{sl}\,dV \tag{5}$$

where $\boldsymbol{r}$ is position vector, $\boldsymbol{\omega}$ denotes angular velocity vector; the subscripts l and s stand for liquid and solid phases; and φ refers to volume fraction corresponding to overlapped volume ($0 \leq \varphi_{sl} \leq 1$).

The principal equations governing solid phase correspond to linear and angular momentum equations:

$$m_s\frac{d\boldsymbol{u}_s}{dt} = \int_V\left(\bar{\rho}\frac{D\bar{\boldsymbol{u}}}{Dt} - \boldsymbol{F}_{p\text{int}}\right)dV + \boldsymbol{F}_{p\text{col}} \tag{6}$$

$$\boldsymbol{I}_s\frac{d\boldsymbol{\omega}_s}{dt} = \int_V \boldsymbol{r}_{sl}\times\left(\bar{\rho}\frac{D\bar{\boldsymbol{u}}}{Dt} - \boldsymbol{F}_{p\text{int}}\right)dV + \boldsymbol{T}_{p\text{col}} \tag{7}$$

where $\boldsymbol{F}_{p\text{col}}$ and $\boldsymbol{T}_{p\text{col}}$ signify solid-solid interaction force/torque vectors, respectively; m and $\boldsymbol{I}_s$ represent mass and moment of inertia tensor computed as:

$$m_s = \int_V \rho_s\,dV \quad ; \quad \boldsymbol{I}_s = \boldsymbol{I}\int_V \rho_s\left|\boldsymbol{r}_{sl}\right|^2 dV \tag{8}$$

where $\boldsymbol{I}$ is unit tensor.

The solid-liquid interaction force term, $\boldsymbol{F}_{p\text{int}}$, is estimated as follows:

$$\boldsymbol{F}_{\text{int}} = \frac{\rho_s\boldsymbol{u}_s' - \overline{\rho\boldsymbol{u}}}{\Delta t} \quad ; \quad \boldsymbol{u}_s' = \boldsymbol{u}_s + \boldsymbol{r}_{sl}\times\boldsymbol{\omega}_s \tag{9}$$

where Δt symbolizes time step size.

Liquid Phase – Enhanced MPS Method

A projection-based fully Lagrangian meshfree method, namely MPS method, is chosen as the fluid solver by considering its distinct superiorities in dealing with violent fluid flow accompanying complex/highly-deformed moving interfaces. In this study, MPS method incorporates a set of enhanced schemes for accuracy and stability (Gotoh, 2018), i.e. the so-called Higher-order Source term of PPE (HS; Khayyer and Gotoh, 2009); Higher-order Laplacian of PPE (HL; Khayyer and Gotoh, 2010); Error Compensating Source term of PPE (ECS; Khayyer and Gotoh, 2011); Gradient Correction (GC; Khayyer and Gotoh, 2011); Dynamic Stabilization (DS; Tsuruta et al., 2013). In addition, the state-of-the-art of particle method for coastal and ocean engineering is introduced in the article by Gotoh and Khayyer (2018).

In the MPS method, the continuity condition is satisfied through solving the PPE (Pressure Poisson Equation), which is derived from Eqs. (1) and (2) based on Chorin's projection method (Chorin, 1968);

$$\left\langle \frac{\Delta t}{\bar{\rho}}\nabla^2 p_{k+1}\right\rangle_i = \frac{1}{n_0}\left(\frac{Dn}{Dt}\right)_i^c - S_{\text{ECS}} \quad ; \quad n_i = \sum_{j\neq i} w_{ij} \tag{10}$$

$$S_{ECS} = \alpha\left[\frac{1}{n_0}\left(\frac{Dn}{Dt}\right)_i^k\right] + \beta\left[\frac{1}{\Delta t}\frac{n_i^k - n_0}{n_0}\right] \tag{11}$$

$$\alpha = \left|\frac{n_i^k - n_0}{n_0}\right| \quad , \quad \beta = \left|\frac{\Delta t}{n_0}\left(\frac{Dn}{Dt}\right)_i^k\right|$$

where k represents the computational time step number, n and n_0 stand for particle number density and initial (reference) particle number density, respectively; w denotes weight function (fifth order Wendland kernel; Wendland, 1995); the superscript c stands for the correction step; the subscripts i and j refer to target particle i and its neighboring particle j. It should be noticed that the second term of right hand side, S_{ECS}, is additional source term of ECS scheme for minimization of the projection-related errors.

The first terms of left and right hand sides are discretized using HL and HS schemes, respectively, as:

$$\left\langle \nabla^2 p_{k+1} \right\rangle_i =$$
$$\frac{1}{n_0} \sum_{j\neq i} \left\{ \frac{\partial p_{ij}}{\partial r_{ij}} \frac{\partial w_{ij}}{\partial r_{ij}} + p_{ij} \left(\frac{\partial^2 w_{ij}}{\partial r_{ij}^2} - \frac{D_s - 1}{r_{ij}} \frac{\partial w_{ij}}{\partial r_{ij}} \right) \right\} \quad (12)$$

$$\left(\frac{Dn}{Dt} \right)_i^c = \sum_{j\neq i} -\nabla w_{ij} \cdot \boldsymbol{u}_{ij}^* \quad (13)$$

where $p_{ij} = p_j - p_i$, $\boldsymbol{r}_{ij} = \boldsymbol{r}_j - \boldsymbol{r}_i$, $r = |\boldsymbol{r}|$ and $\boldsymbol{u}_{ij} = \boldsymbol{u}_j - \boldsymbol{u}_i$; D_s signifies the number of spatial dimensions.

The pressure gradient is calculated by a Taylor-series consistent pressure gradient model (GC) with the stabilizing term (DS), i.e.

$$\left\langle \nabla p \right\rangle_i = \frac{D_s}{n_0} \sum_{j\neq i} \frac{p_j - p_i}{|\boldsymbol{r}_{ij}|^2} \boldsymbol{C}_i \cdot \boldsymbol{r}_{ij} w_{ij} + \frac{1}{n_{0\,i}} \sum_{j\neq i} \boldsymbol{F}_{ij}^{DS} w_{ij} \quad (14)$$

$$\boldsymbol{C}_i = \frac{1}{D_s} \left(\sum_{j\neq i} V_i \frac{\boldsymbol{r}_{ij} \otimes \boldsymbol{r}_{ij}}{|\boldsymbol{r}_{ij}|^2} w_{ij} \right)^{-1} \; ; \; V_i = \frac{1}{\sum_{j\neq i} w_{ij}} \quad (15)$$

$$\begin{cases} \boldsymbol{F}_{ij}^{DS} = 0 & |\boldsymbol{r}_{ij}^*| \geq d_{ij} \\ \boldsymbol{F}_{ij}^{DS} = -\rho_i \Pi_{ij} \frac{\boldsymbol{r}_{ij}}{|\boldsymbol{r}_{ij}|} & |\boldsymbol{r}_{ij}^*| < d_{ij} \end{cases} \quad (16)$$

$$\alpha_{dt} = 1.0 - \alpha_{DS} \; ; \; d_{ij} = \alpha_{DS} \frac{d_i + d_j}{2} \quad (17)$$

$$\Pi_{ij} = \frac{\rho_j}{(\Delta t)^2 (\rho_i + \rho_j)} \left(\sqrt{d_{ij}^2 - |\boldsymbol{r}_{ij\perp}^*|^2} - |\boldsymbol{r}_{ij\parallel}^*| \right) \quad (18)$$

where $\boldsymbol{C}_i$ stands for Gradient Corrective matrix (GC); $\boldsymbol{F}_{ij}^{DS}$ symbolizes a stabilizing force acting on target particle i by its neighboring particle j, Π_{ij} denotes a parameter to adjust the magnitude of $\boldsymbol{F}_{ij}^{DS}$, α_{DS} signifies a constant for adjusting active influence of $\boldsymbol{F}_{ij}^{DS}$, α_{dt} is the Courant number, d refers to the particle diameter, $\boldsymbol{r}_{ij\parallel}^*$ and $\boldsymbol{r}_{ij\perp}^*$ stand for the parallel and normal vectors of $\boldsymbol{r}_{ij}^*$, respectively, i.e. $\boldsymbol{r}_{ij}^* = \boldsymbol{r}_{ij\parallel}^* + \boldsymbol{r}_{ij\perp}^*$.

Solid Phase – Distinct Element Method

The collision forces between a pair of solid particles are modeled by spring-dashpot model (Harada et al., 2008; Harada et al., 2018) on the basis of DEM (Cundall and Strack, 1979). The solid-solid interaction force/torque vectors, $\boldsymbol{F}_{pcol}$ and $\boldsymbol{T}_{pcol}$, are estimated as follows:

$$\boldsymbol{F}_{pcol} = -\sum_{j\in J} (\boldsymbol{T}_{GL})^{-1} \boldsymbol{F}_{pcol,L} \quad (19)$$

$$\boldsymbol{T}_{pcol} = -\frac{d_i}{2} \sum_{j\in J} (\boldsymbol{T}_{GL}')^{-1} \boldsymbol{F}_{pcol,L} \quad (20)$$

$$J = \left\{ j \; \middle| \; |\boldsymbol{r}_{ij}| \leq \frac{d_i + d_j}{2} \right\} \quad (21)$$

where subscript L represents local coordinate of O-$\xi\eta\zeta$; superscript ' stands for transposed matrix; $\boldsymbol{T}_{GL}$ signifies the transformation matrix from the global coordinate of O-xyz to the local coordinate of O-$\xi\eta\zeta$. Solid-solid interaction force vector acting in between target particle i and neighbor particle j with respect to the local coordinate of O-$\xi\eta\zeta$, i.e. $\boldsymbol{F}_{pcol,L}$, is estimated as follows:

$$\boldsymbol{F}_{pcol,L} = \boldsymbol{e} + \boldsymbol{d} \; ; \; \boldsymbol{e} = \boldsymbol{e}^{pre} + k\Delta\boldsymbol{\xi}_{i,j} \; ; \; \boldsymbol{d} = c\Delta\dot{\boldsymbol{\xi}}_{i,j} \quad (22)$$

$$\begin{cases} \langle e_\perp \rangle < 0 & \text{then} & \boldsymbol{F}_{pcol,L} = 0 \\ |\langle e_\parallel \rangle| > \mu_s \langle e_\perp \rangle & \text{then} & \langle \boldsymbol{F}_{pcol,L,\parallel} \rangle = \mu_s \cdot \text{Sign}\left[\langle e_\perp \rangle, \langle e_\parallel \rangle \right] \end{cases} \quad (23)$$

where the subscripts $\perp$ and $\parallel$ represent normal and tangential components of the vector, respectively; the superscript "*pre*" denotes previous time step; $\boldsymbol{e}$ and $\boldsymbol{d}$ signify the inter-element force induced by the spring and dashpot, respectively; k and c stand for the stiffness and damping coefficient; μ_s is the friction coefficient.

SIMULATION SETUP

In the present simulation, a sheetflow regime observing under open channel is simulated using the Lagrange-Lagrange coupling model. The present numerical model is composed of the enhanced Moving Particle Semi-implicit (MPS) model for liquid phase and the distinct element method (DEM) for solid phase. They are employed to calculate liquid and solid phase, respectively for the accurate description of free surface flow and tracking individual solid particle.

The computational setup is determined with reference to the previous experimental setup by Larcher et al. (2007). In the experiment of Larcher et al. (2007), the inclined water channel with 6m length and with 20cm
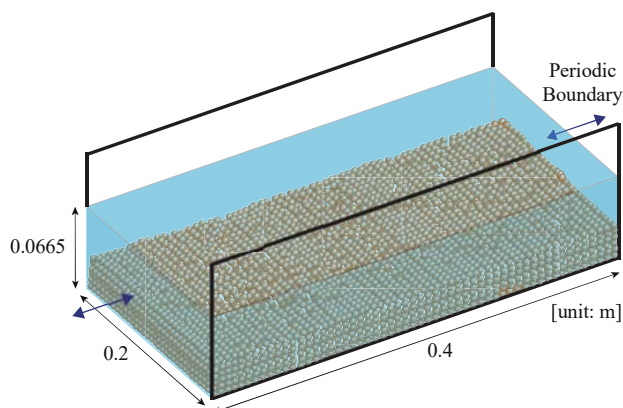
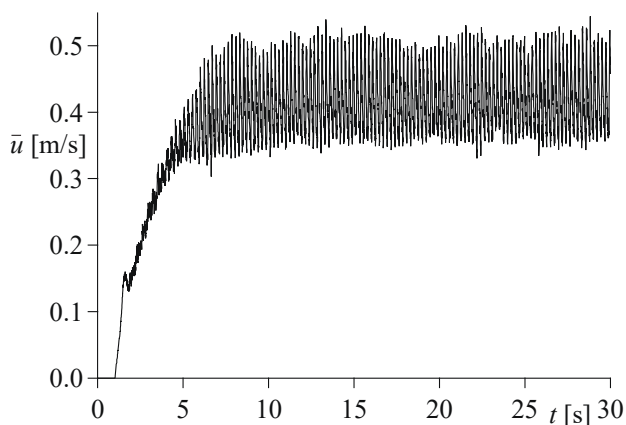Fig. 1 Schematic illustration of initial computational setup

Fig. 2 Time variation of cross-sectional average horizontal velocity

Fig. 3 Typical snapshots of DEM particles together with horizontal velocity field at t = 1 s, 2 s, 5 s, 10 s, 20 s, and 30 s

width was used. The schematic diagram of computational domain is shown in Figure 1. Due to the limitation of computational resources, restricted computational domain is employed. Namely, by considering existence of an immobile bed in the experimental results, a deep part of depositional layer not affecting structures of the sheetflow layer is omitted. Also, by introducing a periodic boundary condition in the flow direction, the length of computational channel is saved.

Although, in the previous experiments by Larcher et al. (2007), cylindrical particles were used to compose movable bed, in the present simulation, spherical DEM solid particles are used for simplicity. The property of each spherical DEM solid particle is with 3.5mm in diameter and with 1.54 in specific density. In addition, the diameter of MPS water particle is 3.5mm. The number of DEM and MPS particles are 98,318 and 123,462, respectively.

From the difficulty in simulating an internal friction angle of the cylindrical particles with using the spherical DEM particles, by restriction of rotational motions of the DEM particles, the internal friction angle is represented in the present simulation. The coefficient of friction is
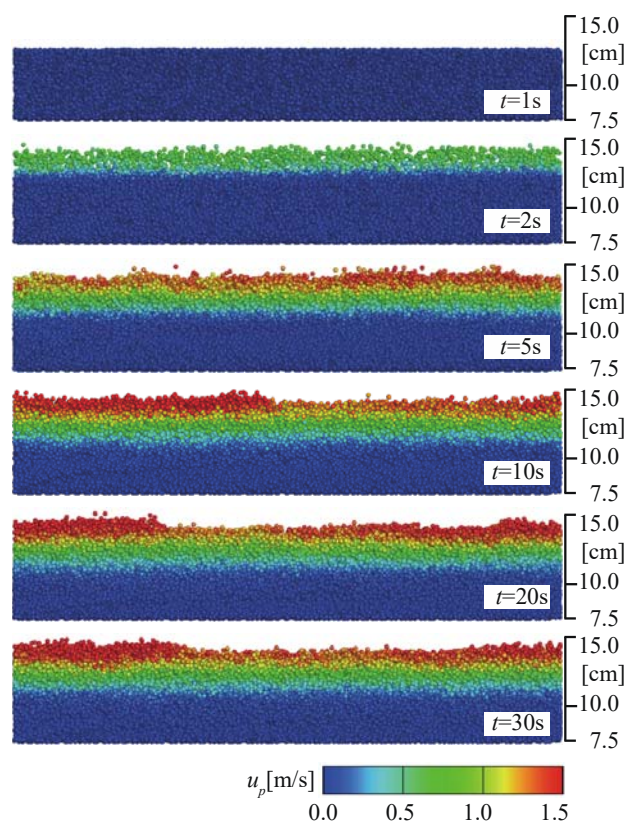
optimized to show good agreement with the previous experimental results by Larcher et al. (2007) in the average and fluctuated particle velocity distribution as shown in the later part of this paper. Specifically, the coefficient of friction from the depositional layer to the sheetflow layer is given by linear interpolation from 0.383(=tan21°) to 0.249(=tan14°) in the present simulation. Note that the definition of the sheetflow layer will be explained in the later part.

VERIFICATION OF NUMERICAL RESULT

The numerical results are compared with the previous experimental results by Larcher et al. (2007), and the validity of the present numerical results will be shown in this section. The experimental results were arranged based on the video image shoot from the side of the water channel. Therefore the information of the motion of the inner particle is not included in the experimental results. By considering the video shooting condition in the experiments just above mentioned, similar counting method to particles is applied in the numerical simulation. In other words, by side viewing from the negative y-direction, only the particles not hidden by other surrounding particles are measured.

Figure 2 shows the time series of the DEM particle averaged velocity of cross sectional plane. After the time
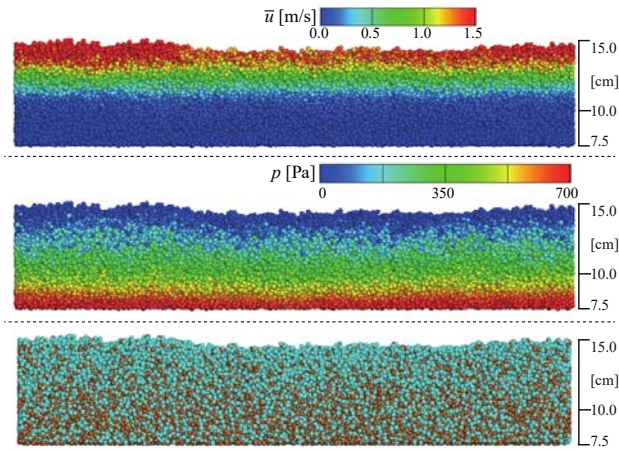
Fig. 4 Typical snapshots of distributions of (a) fluid's horizontal velocity, (b) fluid's pressure and (c) both fluid and DEM particles at t = 30 s
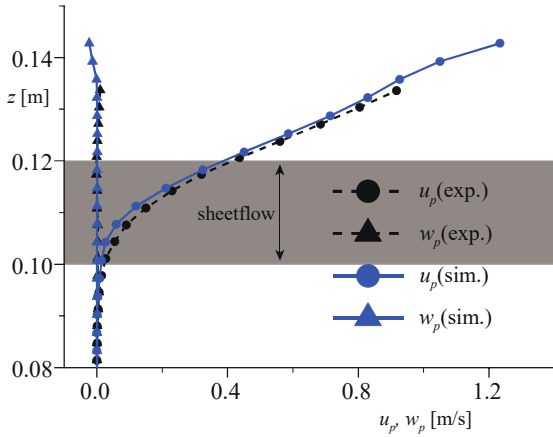

Fig. 6 Concentration profiles of DEM particles

Fig. 5 Average horizontal/vertical velocity profiles of DEM particles
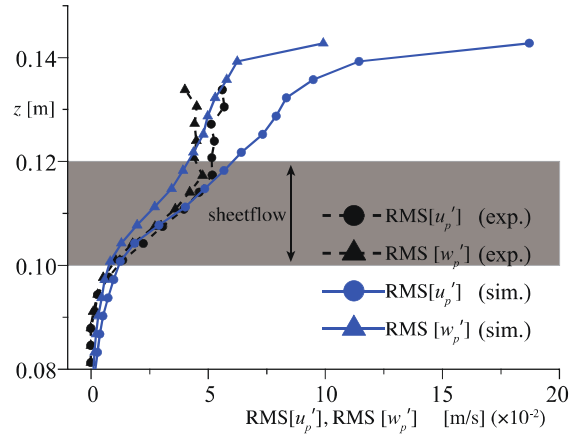
Fig. 7 Horizontal/vertical velocity variation profiles of DEM particles

t=7.0s, although the fluctuating with amplitude of 0.1m/s is shown, the DEM fluidized layer approximately converges to the equilibrium condition. This fluctuation is due to the existence of the waves propagating on the surface of the fluidized layer.

Figure 3 shows the x-wise velocity distribution of the DEM particles viewed from the side wall of the channel. The immobile bed layer is observed in the deep area of the DEM fluidized layer (z<10.0cm). On the other hand, the DEM particles with high velocity are found around the surface of DEM fluidized layer. The DEM velocity increases with time and a wave crest with high particle velocity is confirmed (see after the time t=10s).

Figure 4 shows the velocity and pressure distribution of the MPS particles at the time t=30.0s. The snapshot with blue colored MPS particles and brown colored DEM particles is also shown in Figure 4. In comparing with the velocity distribution of DEM particles as shown in Figure 3, difference between MPS and DEM particles is slight. In addition, the snapshot indicates DEM fluidized layer with well mixed DEM and MPS particles.
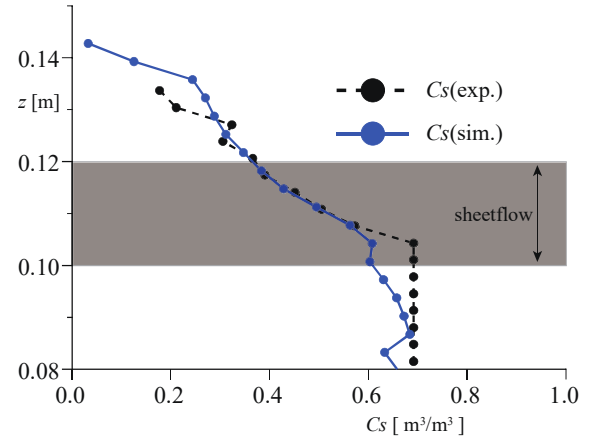
Figure 5 shows the x- and z-wise average velocity profiles of DEM particles in the vertical direction. The present numerical results reasonably agree with the previous experimental results from the viewpoints of the velocity magnitude and position of an inflection point. The vertical profile of the DEM volumetric concentration Cs is shown in Figure 6. The DEM volumetric concentration is estimated using the following equation with the same manner of Larcher et al. (2007).

$$C_S = V_p \left(\frac{k_0}{A\chi} \right)^{1.5} \tag{24}$$

where, V_p is the volume of the DEM particles, k_0 is the number of DEM particles, A is the measurement area, and χ is the correction factor ranging from 0.91 to 0.93 (= 0.93, in this study). Reasonable agreement between the simulation and the experiment is confirmed also in the volumetric concentration. Figure 7 indicates the root-mean-square fluctuation velocities in the x- and z-wise directions. Good agreement between the simulation and the experiment is found in the both components of
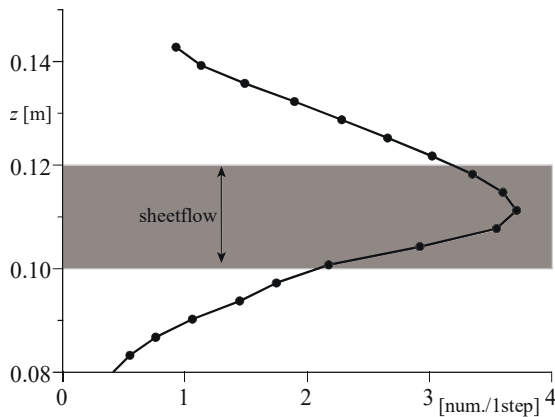
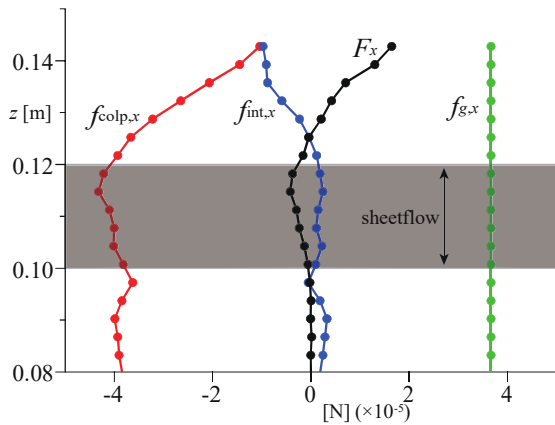Fig. 8 Profiles of number of collisions between DEM particles

Fig. 10 Profiles of total horizontal/vertical forces acting on DEM particles

Fig. 9 Profiles of horizontal forces acting on DEM particles

fluctuation velocities ranging from the immobile bed (z=0.10m) to the height z=0.12m. However, in the area higher than the z=0.12m, the significant discrepancy is found between them. This difference would be attributable to the effect of waves propagation in fluidized layer. Here, in the fluctuation velocities profile, the range from the inflection point to the height showing the good agreement with experimental result is defined as the range of sheetflow layer, in the present study. In this defined sheetflow range, the simulation results reasonably accord with the experimental results in the DEM velocity, fluctuation velocity, and volume concentration. The defined sheetflow range is shown with gray color to indicate the sheetflow area clearly in the profiles.

INNER STRUCTURE OF SHEETFLOW LAYER

Figure 8 shows the vertical profile of DEM particle collision frequency. In the sheetflow region ranging from z=0.10m to z=0.12m, the peak of collisional frequency is found. On the other hand, in the inactive mobile layer between the immobile bed and sheetflow layer, the collision frequency decreases with depth. In the inactive
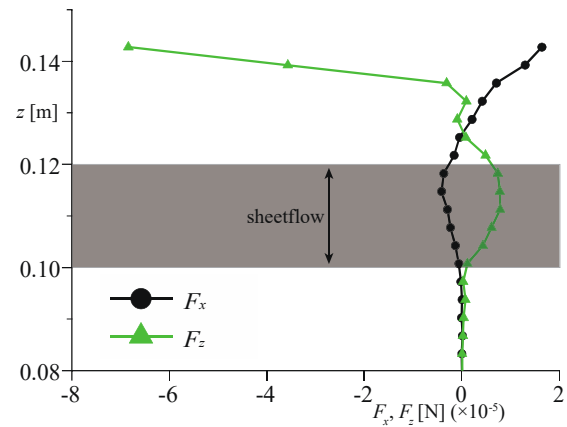
mobile layer, the volumetric concentration of DEM particles is higher than that of the sheetflow layer, therefore, a part of DEM particles flow with keeping contact with surrounding DEM particles condition. The volumetric concentration of DEM particles decreases with an increase of the height, consequently, the gap between DEM particles increase. This increase results in the increase of collision frequency in the sheetflow layer. Meanwhile, in the upper part of sheetflow layer, the volumetric concentration of the DEM particles further decreases. Thus, such decrease of the number of DEM particles causes the decrease of the collision frequency in the upper part of sheetflow layer.

The vertical profiles of forces of each component exerted on DEM particles in x-wise direction are shown in Figure 9, where, f_{clop}: inter-particle force, f_{int}: fluid force, and f_g: gravitational force. In the x-wise direction of Figure 9, the inter-particle force in the height less than the sheetflow layer shows negative value due to the frictional forces between contacting DEM particles. On the other hand, in the height above sheetflow layer, the absolute value of the inter-particle force decreases accompanying the decrease of volumetric concentration of DEM particles. In the vertical profile of fluid force in the x-wise direction, in the height less than sheetflow layer, fluid force is almost zero, because of the high volumetric concentration of DEM particles. In the upper part of sheetflow layer, fluid forces meanwhile act on the DEM-particles in the negative, or opposite, of the gravitational direction.

Figure 10 depicts profile of the resultant forces in x- and z-wise directions. The active motion of DEM particles is inferred in the fluidized layer which is higher than the z=0.10m. Locally the resultant force is not balanced, as found around the surface. However, on average viewpoint of the fluidized layer, a clockwise moment and anticlockwise moment are acted on the fluidized layer, and they are approximately balanced.
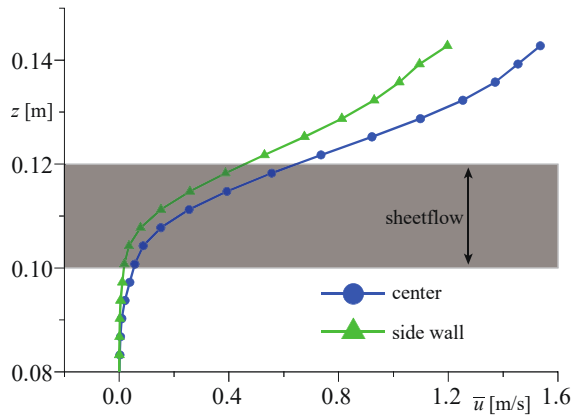
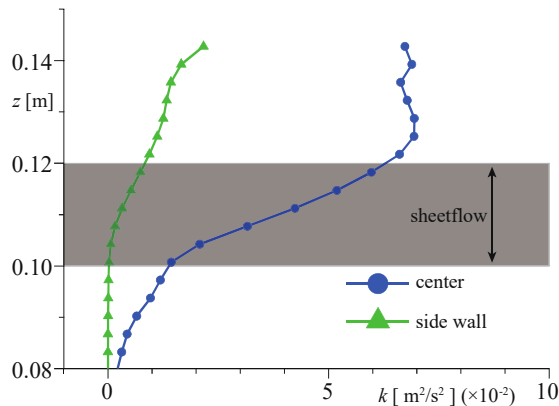Fig. 11 Horizontal velocity profiles of DEM particles measured at center and in the vicinity of side wall

Fig. 12 Profiles of turbulent kinetic energy of DEM particles at center and in the vicinity of side wall

This would be one of the evidences the computed condition is in the equilibrium.

EFFECT OF SIDE WALL OF WATER CHANNEL

The behavior of fluidized layer is compared between close to the side wall of water channel and center of the water channel. Figure 11 shows the vertical profile of MPS particle velocity in the *x*-wise direction under the equilibrium condition. The vertical profile of MPS particles in vicinity of the side wall of the water channel shows slightly thin distribution compared to that of the center plane of water channel. The side wall of water channel confines the motion of MPS particles, thus, the MPS particles around side wall are suppressed their free active motion.

The vertical profiles of turbulent energy and Reynolds stress of the MPS particles at the time *t*=30s are shown in Figures 12 and 13, respectively. The turbulent energy, *k*, and Reynolds stress, *R*, are estimated according to the following equations:

$$k = \frac{1}{2}\left(u'^2 + v'^2 + w'^2\right) \tag{25}$$
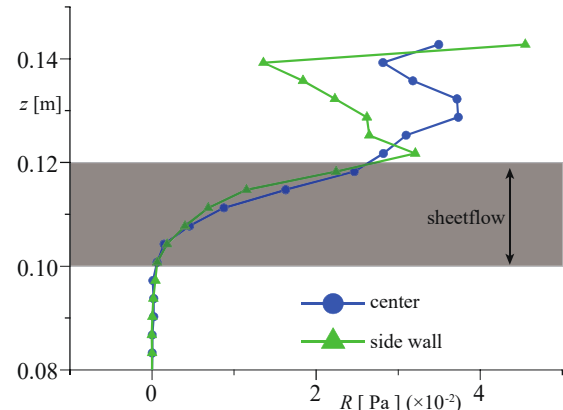
$$R = -\rho u'v' \tag{26}$$

Fig. 13 Profiles of Reynolds stress measured at center and in the vicinity of side wall

where *u*, *v*, *w* are the components of velocity vector **u** i.e. **u** = (*u*, *v*, *w*); the superscript ′ stands for fluctuation quantity.

In both profiles, as well as the velocity profile of DEM particles, the suppressed vertical profiles compared to the center plane of water channel are clearly found. Also, it shows momentum exchange will be attenuated owing to the restriction of momentum transfer by the side wall.

These results suggest the difficulty in reasonable prediction of the inner structure of sheetflow layer using information from side wall.

CONCLUSIONS

In the present study, as the first step of the investigation for sediment transport mechanism under sheetflow regime in a coastal surf-zone, a numerical simulation for sheetflow under uniform flow condition is performed using the DEM-MPS method. The numerical results are verified by comparison with the previous experimental results by Larcher et al. (2007), from the viewpoint of vertical profiles regarding the averaged, fluctuated sediment particle velocity and sediment particle concentration. Then the inner structure of sheetflow layer is numerically investigated from vertical profiles for the forces acting on movable bed particles and index of collision frequency between movable bed particles.

By using numerical data in the sheetflow layer defined with the height of focal point in fluctuated velocities of movable bed DEM particles, both of the high frequency of collision of DEM particles and the high magnitude of inter-particle force between DEM particles are clearly shown in the region of sheetflow layer. Accordingly, the importance of evaluation of inter-particle forces is suggested to investigate the inner structure of sheetflow layer.

To reveal the inner structure of sheetflow layer with experimental measurements will be considerably difficult. However, when the numerical code with high reproducibility is developed, such a powerful numerical code allows us to readily measure the 3-dimensional numerical sheetflow layer. In the present numerical results, due to the restriction of motion of fluidized layer in the side wall direction, the difference is remarkably shown in the fluidized structure of sheetflow layer between the vicinity of side wall of water channel and center of movable bed, and that indicates the importance of wall effects to the investigation of sheetflow layer is numerically shown.

ACKNOWLEDGEMENTS

REFERENCES

Calantoni, J., Puleo, J. A. and Holland, K. T. (2006). Simulation of sediment motions using a discrete particle model in the near surf and swash-zones. Continental Shelf Research 26: 610-621.

Chorin, A.J. (1968). Numerical solution of the Navier-Stokes equations. Math. Comp. 22: 745-762.

Cundall, P. A. and O. D. L. Strack. (1979). A Discrete Numerical Model for Granular Assemblies. Geotechnique 29: 47–65.

Drake, T. G. and Calantoni, J. (2001). Discrete particle model for sheet flow sediment transport in the nearshore. Journal of Geophysical Research: Oceans, 106(C9), 19,859-19,868.

Gotoh, H., Tsuruta, N., Harada, E., Ikari, H. and Kubota, H. (2012). High-Resolution DEM-MPS Methods for Solid-Liquid Multi-Phase Flow. Proceedings of Coastal Engineering, JSCE B2–68(2): 21–25. in Japanese.

Gotoh, H. and Okayasu, A. (2017). Computational Wave Dynamics for Innovative Design of Coastal Structures. Proceedings of the Japan Academy, Series B, Physical and Biological Sciences 93 (8): 525–546.

Gotoh, H. (2018). Ryushiho, Morikita, Shuppan, ISBN-10: 4627922310. (in Japanese)

Gotoh, H. and Khayyer, A. (2018). On the state-of-the-art of particle methods for coastal and ocean engineering. Coastal Engineering Journal, 60, 79-103.

Harada, E. and Gotoh, H. (2008). Computational mechanics of vertical sorting of sediment in sheetflow regime by 3D granular material model. Coastal Engineering Journal 50(1): 19-45.

Harada, E., Gotoh, H. and Tsuruta, N. (2015). Vertical sorting process under oscillatory sheet flow condition by resolved discrete particle model. Journal of Hydraulic Research 53(3): 332-350.

Harada, E., Ikari, H., Shimizu, Y., Khayyer, A. and Gotoh, H. (2019). Numerical Investigation of the Morphological Dynamics of a Step-and-Pool Riverbed Using DEM-MPS. Coastal Engineering Journal, 61(1), 2-14.

Harada, E., Ikari, H., Khayyer, A. and Gotoh, H. (2018). Numerical simulation for swash morphodynamics by DEM–MPS coupling model. Journal of Hydraulic Engineering 144(1): 04017058.

Khayyer, A. and Gotoh, H. (2009). Modified Moving Particle Semi-implicit methods for the prediction of 2D wave impact pressure. Coastal Engineering 56: 419-440.

Khayyer, A. and Gotoh, H. (2010). A Higher Order Laplacian Model for Enhancement and Stabilization of Pressure Calculation by the MPS Method. Applied Ocean Research 32(1): 124-131.

Khayyer, A. and Gotoh, H. (2011). Enhancement of Stability and Accuracy of the Moving Particle Semi-implicit Method. Journal of Computational Physics 230: 3093-3118.

Larcher, M., Fraccarollo, L., Armanini, A. and Capart, H. (2007). Set of measurement data from flume experiments on steady uniform debris flows. Journal of Hydraulic Research 45 Extra Issue, 59-71.

Tsuruta, N. (2014). Improved particle method with high-resolution and computational stability for solid-liquid two-phase flows. Ph.D. Dissertation, 123, Kyoto University.

Tsuruta, N., Khayyer, A. and Gotoh, H. (2013). A Short Note on Dynamic Stabilization of Moving Particle Semi-implicit Method. Computers & Fluids 82: 158-164.

Wendland, H. (1995). Piecewise polynomial, positive definite and compactly supported radial functions of minimal degree. Advances in Computational Mathematics 4: 389-396.